Dynamically encircling exceptional points for robust eigenstate generation and all-optical logic operations in a three-dimensional photonic chip

Chu Li,[1,2] Meng Li,[1,2] Ruiqi Wang,[1,2] Yang Chen,[3,4] Xifeng Ren,[3,4] Linyu Yan,[1,2] Qiang Li,[1,2] Qihuang Gong,[1,2,5,6,7] and Yan Li[1,2,5,6,7,*]

[1]*State Key Laboratory for Mesoscopic Physics and Frontiers Science Center for Nano-optoelectronics, School of Physics, Peking University, Beijing 100871, China*

[2]*Frontiers Science Center for Nano-Optoelectronics, Peking University, Beijing 100871, China*

[3]*CAS Key Laboratory of Quantum Information, University of Science and Technology of China, Hefei 230026, China*

[4]*CAS Center for Excellence in Quantum Information and Quantum Physics, University of Science and Technology of China, Hefei 230026, China*

[5]*Collaborative Innovation Center of Extreme Optics, Shanxi University, Taiyuan, Shanxi 030006, China*

[6]*Hefei National Laboratory, Hefei 230088, China*

[7]*Peking University Yangtze Delta Institute of Optoelectronics, Nantong 226010, China*

(Received 11 October 2023; accepted 1 February 2024; published 26 February 2024)

Dynamically encircling exceptional points (EEPs) in non-Hermitian systems have been utilized to realize robust on-chip mode conversions by taking the advantage that the output states are usually fixed and independent of the input states. This highly protects one of the specific eigenstates, but restricts their practical applications requiring superposition states. Here, we realize an on-chip robust eigenstate generator using a depth-varying 3D waveguide to overpass the EEP system. It not only preserves the robustness of the EEP system to generate one determinate eigenstate, but also generates another two-level eigenstate and arbitrary superposition states. Furthermore, by ingeniously combining two identical generators with a symmetric Y combiner, both the all-optical XOR and OR logic operations insensitive to the variations in the input light are realized by the destructive or constructive interference between the two generators' near-neighboring output signals. This paper paves the way for applications of EEP systems to highly robust state manipulations and information processing in integrated photonic and quantum devices.

DOI: 10.1103/PhysRevResearch.6.013203

I. INTRODUCTION

The exceptional points (EPs) [1,2] in non-Hermitian systems have garnered great interest due to the simultaneous coalescence of eigenvalues and eigenstates, resulting in fundamentally different state evolution compared to traditional Hermitian systems [3–5]. Novel physical phenomena and applications have been investigated in photonic platforms [6–23] including microcavities [24], photonic crystals [25], and coupled waveguide structures [7–9,11–15,20,21,26].

One of the most fascinating phenomena is the dynamical encircling of EPs in parameter spaces by tuning two different parameters [6–16,20,21,27,28]. This results in chiral mode transitions and have been theoretically and experimentally demonstrated in two-level coupled waveguide systems [6,8,9,21,27,28]. The encircling exceptional point (EEP) systems exhibit high robustness of the state transformations, in which the output state is determined solely by the encircling direction. Additionally, the higher-order EPs and the efficiency of the state transformations have also been studied recently [20,29]. There have been already numerous applications based on EEP principles, including asymmetric mode converters [6,15,21,26] and on-chip polarizers [9,20].

Previous studies mainly focused on the mode conversions within the two-level EEP systems themselves because it is challenging to realize robust state manipulations since the output state in an EEP system is usually fixed as one of the eigenstates of the two-level system and remains independent of the input state for a determined encircling direction. It cannot generater another eigenstate without switching the encircling direction, which means light should propagate in a reversed direction. As a result, the EEP systems are hard to integrate in the 2D case to realize robust state manipulations required in the photonic devices, such as the generation of superposition states and the on-chip all-optical logic operations [16,28,30]. Therefore, a new design that can maintain the robustness of the EEP system and perform state operations is desired.

In this paper, we develop a robust on-chip two-level eigenstate generator with a unique 3D configuration inside borosilicate glass by utilizing the 3D direct writing capability of the femtosecond laser [31,32]. It combines a two-level

*li@pku.edu.cn

waveguide EEP system with a depth-varying waveguide overpassing the EEP system. It not only preserves the robustness of the EEP system to generate one determinate eigenstate [33], but also generates another eigenstate. The independent control of the two eigenstates makes it possible to generate arbitrary superposition states by controlling the power ratio and the phase difference of two input paths. Furthermore, by integrating two such generators with a symmetric Y-shaped combiner, on-chip all-optical XOR and OR logic operations are realized by the destructive or constructive interference between the two generators' near-neighboring output signals. In contrast to traditional all-optical logic operations without the EEP systems [34–36], these operations are highly insensitive to the variations in the input beam parameters, such as the wavelength and the polarization. This insensitivity further highlights the advantages of EEP systems for more complex state manipulations and information processing in 3D integrated photonic and quantum devices. It also provides a promising platform to explore the physics in the combination of non-Hermitian and Hermitian systems.

II. THE ON-CHIP 3D GENERATOR OF THE TWO-LEVEL EIGENSTATES

We first analyze the state transformations in the conventional EEP system made up of two waveguides with a length $L = 16$ mm labeled as WG I with the z-dependent loss and WG II with the z-dependent propagation constant as shown in Fig. 1(a). The distance between them is fixed at $d = 10.5$ μm, corresponding to a coupling strength of $\kappa = 0.39$ mm^{-1} for the horizontally polarized light with a wavelength of 785 nm. Scatterers with varying distances are rewritten in WG I to obtain a loss modulation $g_I(z)$, as shown in the upper $g_I - z$ relationship in Fig. 1(b). During the fabrication of WG II, the writing speed is continuously changed to modulate the propagation constant in the z direction, as shown in the lower $\beta_{II} - z$ relationship in Fig. 1(b) (see Appendix for detailed fitting relationships). These two z-dependent parameters $g_I(z)$ and $\beta_{II}(z)$ form a closed loop in the parameter space. It encircles the EP located at (0,2) as shown in the following, enabling the chiral state transformation between the two-level eigenstates.

By defining the path-encoded input orthogonal states as $|0\rangle = (1, 0)^T$ and $|1\rangle = (0, 1)^T$ for light input into the port 0 and 1, the two orthogonal eigenstates of the two-level system are the symmetric state $|+\rangle = \frac{\sqrt{2}}{2}(|0\rangle + |1\rangle) = \frac{\sqrt{2}}{2}(1, 1)^T$ and the antisymmetric state $|-\rangle = \frac{\sqrt{2}}{2}(|0\rangle - |1\rangle) = \frac{\sqrt{2}}{2}(1, -1)^T$. Besides, we define the light in the overpass waveguide as an auxiliary state $|A\rangle$.

In waveguide systems where the waveguides are placed at distances from each other such that adjacent waveguides can evanescently couple, the light propagation in such systems consisting of N unit cells can be modeled by applying the tight-binding approximation [37], which leads to a Schrödinger-type equation [38–43],

$$i\frac{d\psi(z)}{dz} + H(z)\psi(z) = 0, \tag{1}$$

where $\psi(z)$ corresponds to the state vector and $H(z)$ is an $N \times N$ Hamiltonian where the diagonal elements denote the complex propagation constant of the waveguide, while the off-diagonal elements represent the coupling strength between waveguides [9]. Therefore, the light propagation exhibits a similar evolution equation of a quantum particle by mapping the time evolution to the propagation length.

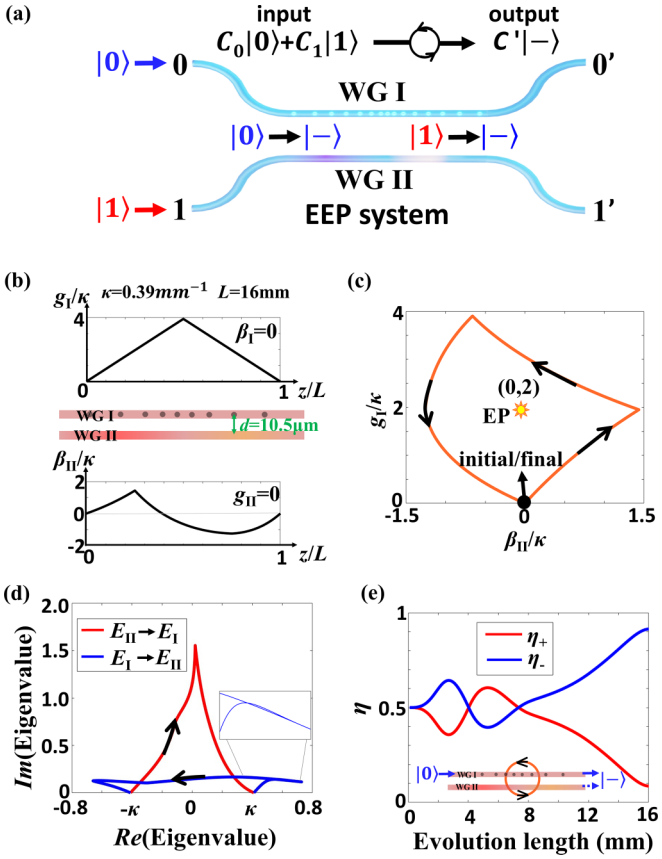

FIG. 1. State transformation in the EEP system. (a) Schematic of the EEP system. For the CCW encircling direction, both the states $|0\rangle$ from the input port 0 and $|1\rangle$ from the input port 1 are transformed into the antisymmetric state $|-\rangle$. For an arbitrary input state $C_0|0\rangle + C_1|1\rangle$, it is still transformed into the antisymmetric state $|-\rangle$ with amplitude C'. (b) Design parameters of the EEP system. The loss $g_I(z)$ varies along the z direction in WG I and the propagation constant $\beta_{II}(z)$ varies in WG II. (c) The CCW encirclement of EP in parameter space, corresponding to the forward propagation of light. (d) The eigenvalues swap with each other after a whole encirclement path. The red curve is the trajectory of the E_{II} to E_I path and the blue curve is the trajectory of the E_I to E_{II} path. (e) Normalized power ratios of symmetric (red curve) and antisymmetric (blue curve) states when light is injected into the WG I.

In the EEP system, the z-dependent Hamiltonian can be expressed as

$$H_{\mathrm{EEP}}(z) = \begin{bmatrix} ig_I(z) & \kappa \\ \kappa & \beta_{II}(z) \end{bmatrix}. \tag{2}$$

Using scaled variables $(\beta_{II}/\kappa, g_I/\kappa)$, the EP is established in parameter space at (0,2), as shown in Fig. 1(c). The counterclockwise (CCW) and the clockwise (CW) encirclements correspond to the light traveling forward and backward, respectively. At the initial/final point or the start/end position of the EEP system, the parameters of the WG I and WG II are identical, so $g_I = g_{II} = 0$ and $\beta_I = \beta_{II} = 0$. As a result, the two

real eigenvalues are $E_I = \kappa$ and $E_{II} = -\kappa$, and the eigenstates are just the symmetric state $|+\rangle$ and the antisymmetric state $|-\rangle$, respectively.

As shown in Fig. 1(d), when the EP is encircled, the two eigenvalues swap with each other after a whole encirclement. For the CCW encircling directions, the value of the E_{II} to E_I path is obviously higher than the E_I to E_{II} path in the imaginary plane during the entire evolution. Thus, the eigenstate $|+\rangle$ experiences much higher loss, and the antisymmetric state $|-\rangle$ eventually dominates. As a result, for an arbitrary input state $C_0|0\rangle + C_1|1\rangle$, the output state of the EEP system is still the antisymmetric state $C'|-\rangle$ with an amplitude C' as shown in Fig. 1(a). Take the case when light is injected into WG I as an example, the calculated normalized power ratio $\eta_\pm = |c_\pm|^2/(|c_+|^2 + |c_-|^2)$ is shown in Fig. 1(e), where c_+ and c_- are the complex amplitude of the symmetric and antisymmetric states, respectively, and $\eta_+(\eta_-)$ corresponds to the symmetric(antisymmetric) state. It is clear that the value of η_- is much higher at the output ports.

The EEP system provides high robustness for the state transformations, but it also bring challenges for the robust state manipulations in integrated devices because any input state is transformed into the antisymmetric state $|-\rangle$ for the CCW direction. The symmetric state $|+\rangle$ cannot be generated without switching the encircling direction, which means the light should propagate in the backward direction of the system. As a result, the EEP systems in two-dimensional structures are hard to generate the arbitrary superposition states required in the photonic devices, making it difficult to integrate.

To overcome this obstacle, we propose the 3D structure of the eigenstate generator using a depth-varying overpass waveguide to generate the symmetric state $|+\rangle$ while preserving the robustness of the EEP system as shown in Fig. 2(a). The generator is fabricated inside borosilicate glass using the femtosecond laser direct writing (FLDW) as shown in Fig. 2(b). It realizes nearly complete transmission of light from port 1 to the overpass waveguide before the EEP system. To block the residual light, scatterers are added at the entrance of WG II in the EEP system. As a result, only the state $|0\rangle$ enters the EEP system and is transformed into the state $|-\rangle$, while the state $|1\rangle$ overpasses the EEP system and turns into the auxiliary state $|A\rangle$, then the state $|A\rangle$ is transformed into the state $|+\rangle$, as demonstrated in the following.

The overpass waveguide couples with other two identical neighboring symmetrically arranged waveguides after the EEP system, where the distance between adjacent waveguides is fixed at 10 μm corresponding to a coupling strength of $\kappa' = 0.45\ \text{mm}^{-1}$ and the coupling length is 2.0 mm. The Hamiltonian of this structure is given by

$$H_{|A\rangle\leftrightarrow|+\rangle} = \begin{bmatrix} 0 & \kappa' & 0 \\ \kappa' & 0 & \kappa' \\ 0 & \kappa' & 0 \end{bmatrix}. \tag{3}$$

According to Eq. (3), the three eigenvalues and corresponding eigenstates are $E_1 = 0$, $\Phi_1 = \frac{\sqrt{2}}{2}(1, 0, -1)^T$ and $E_{2,3} = \pm\sqrt{2}\kappa$, $\Phi_{2,3} = \frac{1}{2}(1, \pm\sqrt{2}, 1)^T$. By applying these results to Eq. (1), we find that the symmetric state $|+\rangle$ and the auxiliary state $|A\rangle$ transform into each other as the light travels, while the antisymmetric state $|-\rangle$ maintains as an eigenstate Φ_1. The coupling strength and the coupling length only affect the amplitudes of the output state as shown in Fig. 2(c). Therefore, the generation of the symmetric state $|+\rangle$ from the state $|A\rangle$ and the preservation of the antisymmetric state $|-\rangle$ from the output of the EEP system are realized.

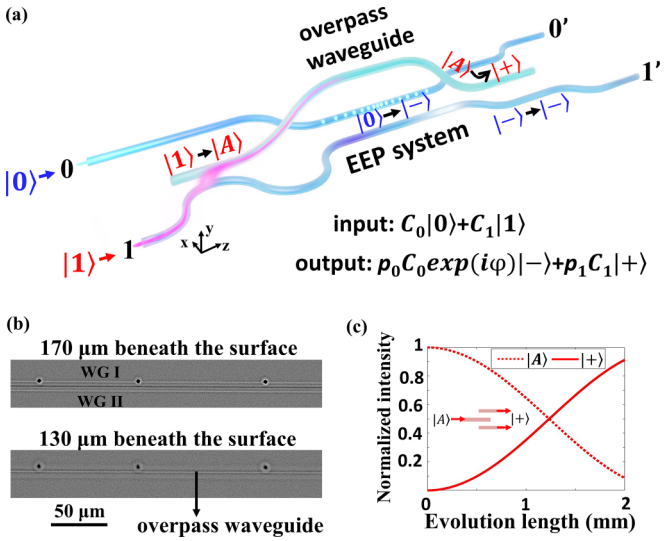

FIG. 2. Working principle of the eigenstate generator. (a) Schematic of the two-level eigenstate generator, which is a 3D integration of the EEP system and the overpass waveguide. The blue and red arrows represent the independent paths of the input state $|0\rangle$ and $|1\rangle$, respectively. When the input state is $|0\rangle$, it enters into the EEP system and is transformed into the antisymmetric state $|-\rangle$, then the state $|-\rangle$ maintains as an eigenstate until it is eventually outputted. While the input state is $|1\rangle$, it first enters into the overpass waveguide and turns into the auxiliary state $|A\rangle$, then the state $|A\rangle$ is transformed into the symmetric state $|+\rangle$ during the coupling between the overpass waveguide and the two identical neighboring symmetrically arranged waveguides. (b) The micrographs of the EEP system with different depth of focus, which demonstrates that the depth-varying waveguide overpasses EEP system without crossing. (c) The intensity of the states $|A\rangle$ and $|+\rangle$ during the coupling between the overpass waveguide and the two identical neighboring symmetrically arranged waveguides.

For an arbitrary input state $|\psi\rangle_{in} = C_0|0\rangle + C_1|1\rangle$, it is transformed to $|\psi\rangle_{out} = p_0C_0\exp(i\varphi)|-\rangle + p_1C_1|+\rangle$, where C_0 and C_1 are the normalized real coefficients of the states $|0\rangle$ and $|1\rangle$ and the values of p_0, p_1, and φ are inherently dependent on the transformation rates. Since the state transformations of the two input ports are independent, it is possible to tune the values of p_0, p_1, and φ by controlling the power ratio and the path difference of the input port 0 and port 1. This advantage enables tunable manipulation of arbitrary input states to realize the robust generation of any desired superposition states of symmetric and antisymmetric states, which are crucial in the study of non-Hermitian systems such as the investigation of the eigenstate conversion efficiency.

III. ROBUST GENERATION OF THE TWO-LEVEL EIGENSTATES AND THE SUPERPOSITION STATES

To verify the function of the robust generation of the two-level eigenstates, we build the experimental setup as shown in

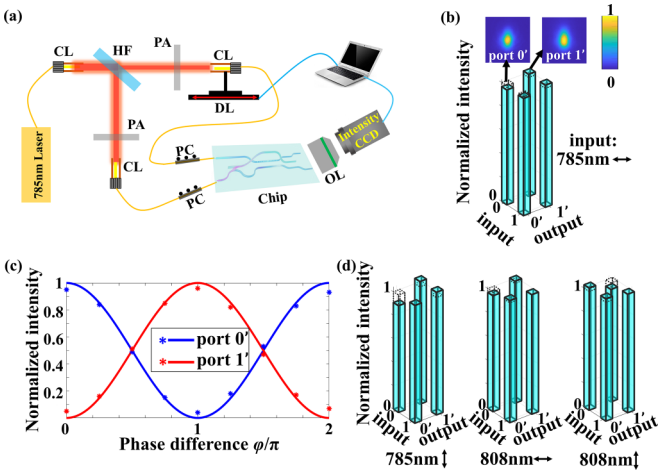

FIG. 3. Experimental results. (a) The experimental setup. (b) Experimental results of single port input. The dashed bars represent the theoretical results. (c) The evolution of normalized intensity of port 0' and port 1' with different values of φ. (d) Experimental results of vertically polarized 785 nm light input and both the horizontally and vertically polarized 808 nm light input. The horizontal (vertical) arrow represents horizontal (vertical) polarization. (Coupling lens, CL; beam splitter, BS; power attenuator, PA; delay line, DL; polarization controller, PC; objective lens, OL.)

Fig. 3(a). The coherent light beam from the laser source is split into two paths by a 50:50 beam splitter. A translation stage with high precision is positioned in one of the two paths to scan the delay line and ensure that the path difference does not exceed the coherent length of the source. The phase difference φ is then adjusted. Two attenuators are placed in the two paths to control the power and thus modify the value of p_0 and p_1 of the structure. With the elimination of the global loss and the phase, the state evolution can be expressed as a transform matrix U that satisfies $|\psi\rangle_{out} = U|\psi\rangle_{in}$,

$$U = \frac{\sqrt{2}}{2}\begin{bmatrix} p_0 e^{i\varphi} & p_1 \\ -p_0 e^{i\varphi} & p_1 \end{bmatrix}. \tag{4}$$

We first inject light to the single port by blocking the light beam in one of the two paths. A horizontally polarized coherent laser with a wavelength of 785 nm is injected into either port 0 or port 1 to create the input state $|0\rangle$ or $|1\rangle$, respectively. The measured output intensity of the port 0' and port 1' exhibit a nearly 1:1 distribution as shown in Fig. 3(b) that agree well with the theoretical results.

Then we construct the superposition input state by changing the power ratio and the phase difference of the two input ports. Without loss of generality, the power ratio of the two optical paths is adjusted to make $p_0 = p_1$ and the phase difference φ is tuned by scanning the delay line. We measure the total output intensity for the single port input case of $|0\rangle$ or $|1\rangle$, respectively, then we tune the two attenuators until the output intensities of the two input states are nearly identical to make $p_0 = p_1$. We prepare the initial state as a superposed state $|\psi\rangle_{in} = \frac{\sqrt{2}}{2}(|0\rangle + |1\rangle)$ by the 50:50 beam splitter and use a fiber array to inject light. Applying the transformation matrix U to it, we can get the final state as $|\psi\rangle_{out} = \frac{1}{2}[(1 + e^{i\varphi})|0\rangle + (1 - e^{i\varphi})|1\rangle]$, thus the intensity of the two output ports are $I_{0'} = \frac{1}{2}(1 + \cos\varphi)$, $I_{1'} = \frac{1}{2}(1 - \cos\varphi)$.

By varying the phase difference φ, the measured output optical intensities within one period of different φ are shown in Fig. 3(c). These results agree well with the calculated values [solid line in Fig. 3(c)].

Conventional devices without EEP systems are always sensitive to variations in input light, such as the wavelength and the polarization. This sensitivity, which arises from the fact that changes of the input parameters lead to alterations in the coupling strength and propagation constants, has a significant impact on the overall performance. On the contrary, the two-level eigenstate generator exhibits a remarkable robustness. As the key part, the EEP system is highly robust to the parameter disturbances due to the unique topological structure in the parameter space as long as the EP remains encircled within the loop, thus the output state is the antisymmetric state $|-\rangle$ from the input state $|0\rangle$. In addition, the scatterers at the entrance of WG II blocks light from entering the EEP system through port 1 and the output state remains the symmetric state $|+\rangle$ from the input state $|1\rangle$.

We conduct various experiments to demonstrate the robustness. Firstly, we input the vertically polarized light, and the measured output intensity at port 0' and port 1' with single port input still shows a nearly 1:1 distribution as shown in the left column in Fig. 3(d). Secondly, by switching the wavelength of the input light to 808 nm, we obtain similar results for both horizontally and vertically polarized light as shown in the center and right columns in Fig. 3(d), which also exhibit a nearly 1:1 distribution. These results indicate that the performance of the generator is highly robust to the variations of the input light, which shows great potential for the EEP system to realize robust state manipulations in broadband and polarization-insensitive devices.

IV. REALIZATION OF THE ROBUST ALL-OPTICAL XOR AND OR OPERATIONS

All-optical logic operations, which usually based on the interference effect, play a crucial role in information processing and communication in optical integrated devices [35]. Conventional all-optical logic operations without EEP systems require extremely accurate manipulations of the dynamical phases thus are sensitive to the deviations of the input light [34,36]. Robust on-chip all-optical logic operation has been realized based on the topological protection [44,45], but it usually requires a photonic lattice or crystal with periodic structures. In contrast, the state transformation in the EEP system exhibits strong robustness using a few waveguides without complex lattice structures and has been proposed for the robust optical logic gates, but to the best of our knowledge, there has been no experimental report.

As demonstrated above, the integration of the EEP system and the 3D overpass waveguide facilitates the robust generation of the two-level eigenstates $|-\rangle$ and $|+\rangle$. The phase difference of the two output ports is 0 for the symmetric state and π for the antisymmetric state, respectively and relatively insensitive to parameter disturbances. Inspired by this characteristic, we fabricate a structure that combines two identical generators through a simple symmetric Y-shaped combiner to

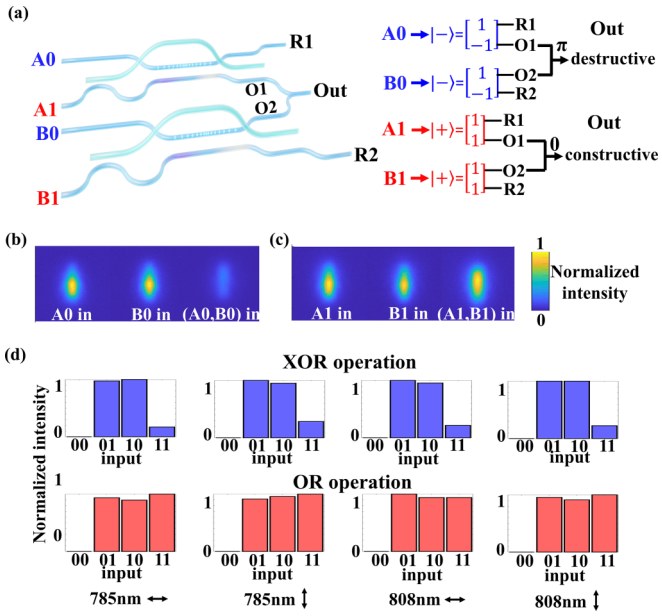

FIG. 4. On-chip robust XOR and OR operations. (a) Schematic diagram of the structure that combines two generators with a Y-shaped combiner. The multiplexing of the XOR and OR operations are shown in the right column. [(b),(c)] The output intensity distributions for both single and superposition inputs at ports A0(A1) and B0(B1), which indicate a XOR(OR) operation. (d) The output intensity for both the horizontally and the vertically polarized light input cases with the wavelength of 785 nm and 808 nm. The top (bottom) four columns represent the case where A0 and B0 (A1 and B1) are the input ports, corresponds to the XOR (OR) operation. The horizontal (vertical) arrow represents horizontal (vertical) polarization.

achieve robust on-chip all-optical logic operations based on the interference between the two generators' near-neighboring output signals as shown in Fig. 4(a).

The four ports A0, B0, A1, and B1 are the input ports, the two near-neighboring output ports of the generators, namely O1 and O2, comprise the two arms of the Y combiner used for interference and the combining path of the Y combiner serves as the output port, with two reference ports R1 and R2. The presence or absence of optical signals at the input or output ports corresponds to the logic state "1" or "0". When two coherent light beams are injected simultaneously into ports A0 and B0 with identical phase, the output states of both generators are $\frac{\sqrt{2}}{2}p_0\exp(i\varphi)(-1,1)^T$ and the phase difference between the two output ports is π. Due to the identical structures of the two generators and the symmetric arms of the Y-combiner, both the global losses and the propagation phases of the two output states are nearly equal. Consequently, the phase difference between the two arms of the Y- combiner (O1 and O2) is π, leading to destructive interference at the output port as shown in the right part in Fig. 4(a). On the other hand, for input ports A1 and B1, the output states are both $|\psi\rangle_{out} = p_1|+\rangle = \frac{\sqrt{2}}{2}p_1(1,1)^T$, thus the phase difference is 0, leading to constructive interference as shown in the right part in Fig. 4(a). As a result, this configuration enables the multiplexing of all-optical XOR and OR logic gates by choosing ports A0 and B0 or A1 and B1 as the input ports. The two operations are insensitive to the variations in the input light as a result of the robustness of the two generators.

In the experiment, we first perform the single port injection, where 785 nm horizontally polarized light is injected into either port A0 or B0 to achieve input logic states of (1,0) or (0,1). The output results are shown in the left and middle parts of Fig. 4(b). Taking into account the potential additional loss from the Y-shaped combiner, here we normalize the output intensity to the total optical intensity of all output ports (i.e., ports R1, R2, and Out).

To realize an input logic state of (1,1), a new series of samples are fabricated with equally arms Y-shaped splitters connecting the ports A0 and B0 that allow simultaneous injection of light into the two ports with equal power and phase. The normalized output result under this condition is shown in the right part of Fig. 4(b). Clearly, under the input condition of logic state (1,1), the optical intensity at the output port is significantly lower compared to the input situations of logic states (1,0) and (0,1), corresponding to the output logic state "0" thus demonstrating the success of the XOR operation. The results for the OR operation are obtained by injecting light into the ports A1 and B1 simultaneously using the similar method, as shown in Fig. 4(c).

To verify the robustness of the all-optical logic operations, we change the wavelength and polarization of the input light beam and the results for these cases are shown in Fig. 4(d). We find that when selecting ports A0 and B0 as input ports, the normalized output intensity under simultaneous injection conditions is significantly lower compared to the single port injection case [as shown in the top row of Fig. 4(d)], demonstrating the successful XOR operation. Conversely, when ports A1 and B1 are chosen as input ports, the normalized output intensity shows minimal variation under simultaneous injection conditions compared to the case of single-port injection [as shown in the bottom row of Fig. 4(d)], indicating the success of the OR operation. These results provide definitive evidence for the robustness of multiplexed XOR and OR operations and further indicate the potential applications of EEP systems to realize robust state manipulations and operations in optical information processing devices.

V. DISCUSSION

In summary, we present a 3D on-chip eigenstate generator consisting of the EEP system and the depth-varying overpass waveguide utilizing femtosecond laser's 3D direct writing capability. The EEP system has high robustness conversion characteristics but is difficult to apply in integrated photonic devices because the output states are usually fixed and independent of the input state. To overcome this limitation, we use the depth-varying waveguide to overpass the EEP system and realize the robust generation of the eigenstates from the path-dependent states. The independent control allows to tune the transformation rates and the phase difference thus enables to generate states with different components of the eigenvectors. Moreover, by combining two such generators with a Y-shaped combiner, we realize the multiplexing of all-optical XOR and OR logic gates. Both the XOR and the

OR operations show strong robustness to the variations of the input light including the wavelength and the polarization. These results indicate great potential applications for encircling exceptional point systems to realize highly robust state manipulations and information processing in integrated broadband and polarization-insensitive photonic and quantum devices. Additionally, our paper offers a promising platform to explore phenomena that combine non-Hermitian and Hermitian structures, paving the way for integrated non-Hermitian photonic chips.

ACKNOWLEDGMENTS

This research was funded by National Natural Science Foundation of China (Grants No. 12134001, No. 11527901, and No. 61590933); National Key Research and Development Program of China (Grants No. 2018YFB1107205 and No. 2016YFA0301302); Joint Fund for Equipment Pre-research Space Science and Technology (Grant No. 6141B06140601) and the Innovation Program for Quantum Science and Technology (Grant No. 2021ZD0301500).

APPENDIX

1. Fabrication of samples

The on-chip two-level eigenstate generator consisting of coupled waveguides are fabricated in borosilicate glass (Eagle XG, Corning) by focusing pulses generated by a regeneratively amplified Yb: KGW femtosecond laser system (Pharos20, Light Conversion) at a wavelength of 1030 nm with a duration of 240 fs, and 1-MHz repetition rate. The microscope objective (20×, NA = 0.4) focus the pulse with a power of 157 nJ at a depth of 170 μm below the glass surface to write straight waveguides, while the depth of the overpass waveguide varies between 130 μm to 170 μm. The small NA objective lens ensures that the cross section of waveguides within a certain depth range is nearly identical and the propagation loss of the straight waveguide is about 0.96 dB/cm. We use a computer-controlled high-precision three-axis air-bearing stage (FG1000, Aerotech) to move the sample at a constant speed of 25 mm/s, except for fabrication of the WG II with a continuously varying speed.

In order to introduce extra losses into WG I, we focus the laser pulses on specific designed sites inside the waveguide with pulse energy of 235 nJ and an exposure time of 0.5 s to create scatterers. These scatterers, spaced sufficiently apart, cause nearly identical losses.

The distance between the two input or output ports is 127 μm to suit the fiber arrays. For the curved segments, the bending radius is set as 80 mm on the x-z plane and 140 mm on the y-z plane to minimize the bending loss and avoid undesired coupling. The height of the overpass waveguides is 40 μm. The total length of the generator is 40 mm.

2. Fitting the parameters of Hamiltonians

There are three critical parameters of Hamiltonians: the coupling strength κ between waveguides, the propagation constants β, and the relative loss g.

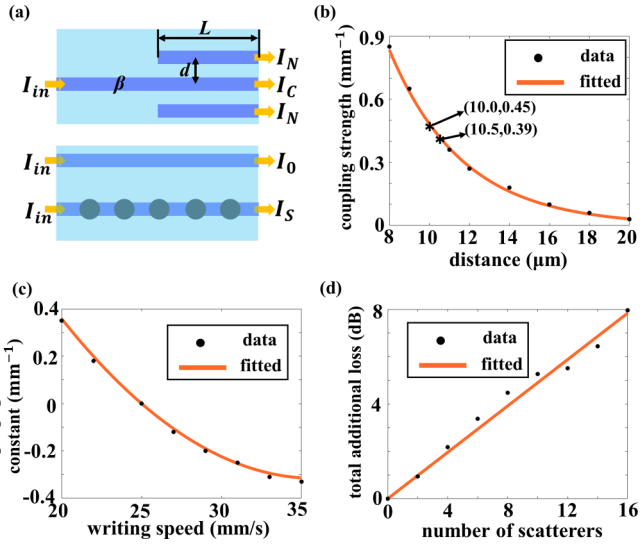

FIG. 5. Schematic of the systems to obtain the fitted parameters and the results. (a) The schematic of the systems to measure the coupling strength, the propagation constants and the extra loss. (b) The relationship between the coupling strength and the distance. (c) The relationship between the propagation constant and the writing speed. (d) The relationship between the total additional loss and the number of scatterers in a 20 mm waveguide.

It is well accepted that the coupling strength is determined by the distance between the neighboring waveguides. To get the relationship, we fabricate several identical triple-waveguide systems, as shown in the upper portion of Fig. 5(a). In these systems, the two side waveguides have a distance of d from the center waveguide, and the coupling length is L. When light is injected into the center waveguide, the output intensities meet $I_C = \cos^2(\sqrt{2}\kappa L)$ and $I_N = \frac{1}{2}\sin^2(\sqrt{2}\kappa L)$. We fabricate several similar structures with different coupling lengths L and fit the corresponding κ for a fixed distance d. Then, we repeat the same process for another d. Finally, based on these results, we obtain the relationship between coupling strength and distance for horizontally polarized light with the wavelength of 785 nm, as shown in Fig. 5(b).

To achieve different propagation constants for the waveguides, the writing speed is varied. We set the propagation constant for the writing speed of 25 mm/s as zero, and a lower (higher) speed resulted in a positive (negative) propagation constant. To get the relationship, we change the writing speed v for the center waveguide in the triple-waveguide systems in Fig. 5(a), thus the center waveguide will acquire a different propagation constant β. In such case, when light is injected into it, the output intensities are $I_C = \cos^2(\frac{\sqrt{\beta^2+8\kappa^2}}{2}L) + \frac{\beta^2}{\beta^2+8\kappa^2}\sin^2(\frac{\sqrt{\beta^2+8\kappa^2}}{2}L)$ and $I_N = \frac{4\kappa^2}{\beta^2+8\kappa^2}\sin^2(\frac{\sqrt{\beta^2+8\kappa^2}}{2}L)$. We fabricate several similar structures with different L for a fixed distance d (where κ is known) and writing speed v, and fit the propagation constant β. Then, we repeat the same steps for another v. Finally, we use the obtained results to deduce the relationship between the propagation constant and the writing speed, as shown in Fig. 5(c). Therefore, by continuously

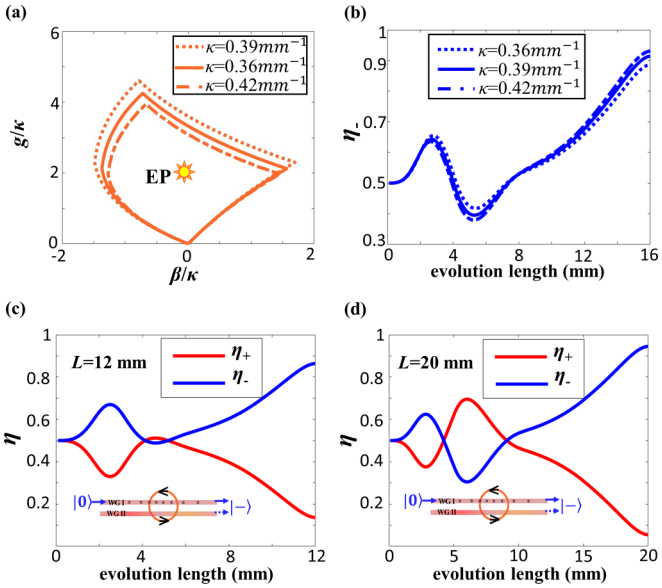

FIG. 6. Results of different coupling strength and length of the EEP system. (a) The trajectories of the loops for three different coupling strengths. (b) The normalized power ratios of the antisymmetric states when light is injected into the WG I for three different coupling strengths. (c) and (d) are the normalized power ratios of the symmetric and antisymmetric states when light is injected into the WG I for $L = 12$ mm and $L = 20$ mm, respectively.

changing the writing speed of the WG II, we can get the $\beta(z)$ according to Fig. 1(b).

To introduce additional loss into the waveguides, we focus laser pulses with an energy of 235 nJ inside a written waveguide and create scatterers with an exposure time of 0.5 s. We compare the output intensity I_S of the waveguide with several evenly spaced scatterers inside it to the output intensity I_0 of the waveguide without scatterers. The additional loss is expressed as $\gamma = -10lg(I_S/I_0)$, and we establish the relationship between the number of scatterers and the total additional loss, as shown in Fig. 5(d), where each scatterer induces an average loss of 0.5 dB. Note that the value of g in the Hamiltonian causes the output intensity to decay to $\exp(-2gL)$ compared to the initial, thus we get $\gamma = -10lg(\exp(-2gL))$ and $g = 0.115\gamma$ with $L = 1$ mm (the unit length). Therefore, by fabricating unevenly distributed scatterers inside the WG I, we can get the $g(z)$ according to Fig. 1(b).

3. Additional calculation results to demonstrate the robustness of the EEP system

The coupling strength between waveguides may vary slightly due to deviations in distance, polarizations, and wavelengths. For the EEP system, changes in coupling strength can cause the trajectory of the loop in Fig. 1(c) to deform. However, here we show that as long as the exceptional point (EP) is dynamically encircled, the output states are highly robust, as demonstrated through numerical calculations.

The evolution of the normalized ratios of antisymmetric states for three different cases are shown in Figs. 6(a) and 6(b). We find that for three different coupling strengths with differences close to 10%, all the normalized power ratios at the output interface remain a high level. These results demonstrate the high robustness of the EEP system to the coupling strength.

For the EEP system, we demonstrate its high robustness to coupling length by presenting results for two different lengths, as shown in Figs. 6(c) and 6(d). The normalized power ratios of the antisymmetric states at the output interface are 87%, 91%, and 95% for the coupling lengths of 12 mm, 16 mm (as utilized in the main text), and 20 mm, respectively. Remarkably, even with a nearly 50% variation in the evolution length, all of these ratios remain close to each other and at a high level.

[1] C. M. Bender and S. Boettcher, Real spectra in non-Hermitian Hamiltonians having *PT* symmetry, Phys. Rev. Lett. **80**, 5243 (1998).
[2] M. Berry, Physics of non-Hermitian degeneracies, Czech. J. Phys. **54**, 1039 (2004).
[3] L. Feng, R. El-Ganainy, and L. Ge, Non-Hermitian photonics based on parity–time symmetry, Nat. Photon. **11**, 752 (2017).
[4] H. Zhao and L. Feng, Parity–time symmetric photonics, Natl. Sci. Rev. **5**, 183 (2018).
[5] K. Ding, C. Fang, and G. Ma, Non-Hermitian topology and exceptional-point geometries, Nat. Rev. Phys. **4**, 745 (2022).
[6] J. Doppler, A. A. Mailybaev, J. Böhm, U. Kuhl, A. Girschik, F. Libisch, T. J. Milburn, P. Rabl, N. Moiseyev, and S. Rotter, Dynamically encircling an exceptional point for asymmetric mode switching, Nature (London) **537**, 76 (2016).
[7] X.-L. Zhang, T. Jiang, and C. T. Chan, Dynamically encircling an exceptional point in anti-parity-time symmetric systems: asymmetric mode switching for symmetry-broken modes, Light Sci. Appl. **8**, 88 (2019).
[8] X.-L. Zhang and C. T. Chan, Dynamically encircling exceptional points in a three-mode waveguide system, Commun. Phys. **2**, 63 (2019).
[9] A. U. Hassan, B. Zhen, M. Soljačić, M. Khajavikhan, and D. N. Christodoulides, Dynamically encircling exceptional points: exact evolution and polarization state conversion, Phys. Rev. Lett. **118**, 093002 (2017).
[10] W. Liu, Y. Wu, C.-K. Duan, X. Rong, and J. Du, Dynamically encircling an exceptional point in a real quantum system, Phys. Rev. Lett. **126**, 170506 (2021).
[11] Q. Liu, S. Li, B. Wang, S. Ke, C. Qin, K. Wang, W. Liu, D. Gao, P. Berini, and P. Lu, Efficient mode transfer on a compact silicon chip by encircling moving exceptional points, Phys. Rev. Lett. **124**, 153903 (2020).
[12] H. Qi, X. Hu, X. Wang, and Q. Gong, Encircling an exceptional point in a multiwaveguide anti–parity-time-symmetry system, Phys. Rev. A **103**, 063520 (2021).
[13] S. Yang, X. Zhang, and H. Sun, Exceptional point protected robust on-chip optical logic gates, Exploration **2**, 20210243 (2022).

[14] Y. Choi, C. Hahn, J. W. Yoon, S. H. Song, and P. Berini, Extremely broadband, on-chip optical nonreciprocity enabled by mimicking nonlinear anti-adiabatic quantum jumps near exceptional points, Nat. Commun. **8**, 14154 (2017).

[15] X. Shu, A. Li, G. Hu, J. Wang, A. Alù, and L. Chen, Fast encirclement of an exceptional point for highly efficient and compact chiral mode converters, Nat. Commun. **13**, 2123 (2022).

[16] Z. Feng and X. Sun, Harnessing dynamical encircling of an exceptional point in anti-PT-symmetric integrated photonic systems, Phys. Rev. Lett. **129**, 273601 (2022).

[17] T. Goldzak, A. A. Mailybaev, and N. Moiseyev, Light stops at exceptional points, Phys. Rev. Lett. **120**, 013901 (2018).

[18] S. Xia, D. Kaltsas, D. Song, I. Komis, J. Xu, A. Szameit, H. Buljan, K. G. Makris, and Z. Chen, Nonlinear tuning of PT symmetry and non-Hermitian topological states, Science **372**, 72 (2021).

[19] H. Nasari, G. Lopez-Galmiche, H. E. Lopez-Aviles, A. Schumer, A. U. Hassan, Q. Zhong, S. Rotter, P. LiKamWa, D. N. Christodoulides, and M. Khajavikhan, Observation of chiral state transfer without encircling an exceptional point, Nature (London) **605**, 256 (2022).

[20] A. Li, W. Chen, H. Wei, G. Lu, A. Alù, C.-W. Qiu, and L. Chen, Riemann-encircling exceptional points for efficient asymmetric polarization-locked devices, Phys. Rev. Lett. **129**, 127401 (2022).

[21] J. W. Yoon, Y. Choi, C. Hahn, G. Kim, S. H. Song, K.-Y. Yang, J. Y. Lee, Y. Kim, C. S. Lee, J. K. Shin *et al.*, Time-asymmetric loop around an exceptional point over the full optical communications band, Nature (London) **562**, 86 (2018).

[22] M. Abbasi, W. Chen, M. Naghiloo, Y. N. Joglekar, and K. W. Murch, Topological quantum state control through exceptional-point proximity, Phys. Rev. Lett. **128**, 160401 (2022).

[23] A. Schumer, Y. G. N. Liu, J. Leshin, L. Ding, Y. Alahmadi, A. U. Hassan, H. Nasari, S. Rotter, D. N. Christodoulides, P. LiKamWa, and M. Khajavikhan, Topological modes in a laser cavity through exceptional state transfer, Science **375**, 884 (2022).

[24] C. Dembowski, H.-D. Gräf, H. L. Harney, A. Heine, W. D. Heiss, H. Rehfeld, and A. Richter, Experimental observation of the topological structure of exceptional points, Phys. Rev. Lett. **86**, 787 (2001).

[25] S. Weimann, M. Kremer, Y. Plotnik, Y. Lumer, S. Nolte, K. G. Makris, M. Segev, M. Rechtsman, and A. Szameit, Topologically protected bound states in photonic parity–time-symmetric crystals, Nat. Mater. **16**, 433 (2017).

[26] S.-R. Yang, X.-L. Zhang, and H.-B. Sun, Design of a non-Hermitian on-chip mode converter using phase change materials, Opt. Lett. **45**, 4630 (2020).

[27] C. Dembowski, B. Dietz, H.-D. Gräf, H. L. Harney, A. Heine, W. D. Heiss, and A. Richter, Encircling an exceptional point, Phys. Rev. E **69**, 056216 (2004).

[28] F. Yu, X.-L. Zhang, Z.-N. Tian, Q.-D. Chen, and H.-B. Sun, General rules governing the dynamical encircling of an arbitrary number of exceptional points, Phys. Rev. Lett. **127**, 253901 (2021).

[29] I. Mandal and E. J. Bergholtz, Symmetry and higher-order exceptional points, Phys. Rev. Lett. **127**, 186601 (2021).

[30] Y. Chen, X.-T. He, Y.-J. Cheng, H.-Y. Qiu, L.-T. Feng, M. Zhang, D.-X. Dai, G.-C. Guo, J.-W. Dong, and X.-F. Ren, Topologically protected valley-dependent quantum photonic circuits, Phys. Rev. Lett. **126**, 230503 (2021).

[31] K. M. Davis, K. Miura, N. Sugimoto, and K. Hirao, Writing waveguides in glass with a femtosecond laser, Opt. Lett. **21**, 1729 (1996).

[32] A. Szameit and S. Nolte, Discrete optics in femtosecond-laser-written photonic structures, J. Phys. B: At., Mol. Opt. Phys. **43**, 163001 (2010).

[33] M. Li, C. Li, Y. Chen, L.-T. Feng, L. Yan, Q. Zhang, J. Bao, B.-H. Liu, X.-F. Ren, J. Wang, S. Wang, Y. Gao, X. Hu, Q. Gong, and Y. Li, On-chip path encoded photonic quantum Toffoli gate, Photon. Res. **10**, 1533 (2022).

[34] Y. Fu, X. Hu, C. Lu, S. Yue, H. Yang, and Q. Gong, All-optical logic gates based on nanoscale plasmonic slot waveguides, Nano Lett. **12**, 5784 (2012).

[35] Y. Chen, Y. Cheng, R. Zhu, F. Wang, H. Cheng, Z. Liu, C. Fan, Y. Xue, Z. Yu, J. Zhu *et al.*, Nanoscale all-optical logic devices, Sci. China Phys. Mech. Astron. **62**, 44201 (2019).

[36] H. Wei, Z. Wang, X. Tian, M. Käll, and H. Xu, Cascaded logic gates in nanophotonic plasmon networks, Nat. Commun. **2**, 387 (2011).

[37] Y. Chen, X. Chen, X. Ren, M. Gong, and G.-C. Guo, Tight-binding model in optical waveguides: Design principle and transferability for simulation of complex photonics networks, Phys. Rev. A **104**, 023501 (2021).

[38] S. Longhi, Quantum-optical analogies using photonic structures, Laser Photon. Rev. **3**, 243 (2009).

[39] M. Segev, Y. Silberberg, and D. N. Christodoulides, Anderson localization of light, Nat. Photon. **7**, 197 (2013).

[40] Q. Liu, W. Liu, K. Ziegler, and F. Chen, Engineering of Zeno dynamics in integrated photonics, Phys. Rev. Lett. **130**, 103801 (2023).

[41] C. Li, M. Li, L. Yan, S. Ye, X. Hu, Q. Gong, and Y. Li, Higher-order topological biphoton corner states in two-dimensional photonic lattices, Phys. Rev. Res. **4**, 023049 (2022).

[42] X.-L. Zhang, F. Yu, Z.-G. Chen, Z.-N. Tian, Q.-D. Chen, H.-B. Sun, and G. Ma, Non-Abelian braiding on photonic chips, Nat. Photon. **16**, 390 (2022).

[43] L.-C. Wang, Y. Chen, M. Gong, F. Yu, Q.-D. Chen, Z.-N. Tian, X.-F. Ren, and H.-B. Sun, Edge state, localization length, and critical exponent from survival probability in topological waveguides, Phys. Rev. Lett. **129**, 173601 (2022).

[44] W. Liu, M. Hwang, Z. Ji, Y. Wang, G. Modi, and R. Agarwal, Z_2 photonic topological insulators in the visible wavelength range for robust nanoscale photonics, Nano Lett. **20**, 1329 (2020).

[45] L. He, H. Y. Ji, Y. J. Wang, and X. D. Zhang, Topologically protected beam splitters and logic gates based on two-dimensional silicon photonic crystal slabs, Opt. Express **28**, 34015 (2020).